Flow at ice-divide triple junctions: 1. Three-dimensional full-Stokes modeling

Fabien Gillet-Chaulet[1] and Richard C. A. Hindmarsh[1]

Received 12 January 2010; revised 8 February 2011; accepted 14 April 2011; published 30 June 2011.

[1] Ice domes are either axisymmetric, high points along ridges, or ridge triple junctions. We model time-dependent isothermal flow near triple junctions, solving the full set of mechanical equations with a nonlinear power law rheology. Forcing is applied through the boundary conditions, which affect flow patterns at outlets. Where such forcing is purely axisymmetric, an axisymmetric dome is formed. If a threefold symmetry in the forcing is applied, the axisymmetric dome breaks up into three ridges subtending angles of 120°. Sets of experiments where the forcing was not exactly threefold symmetric by angle or by amplitude caused the triple junction to migrate to a new steady state. Here, in steady state, the ridges join the triple junction at nearly 120°, but one ridge curves to satisfy the boundary forcing. The slope pattern in the immediate dome vicinity depends only on a dimensionless parameter, which is a function of the ice consistency, the accumulation, and the rheological power law index. Attempts to replicate the topography around Summit, Greenland, obtained a good fit with $n = 3$. At a triple junction the dome is really distinct from the surrounding ridges, contrary to the highest point of a single ridge divide. As a consequence, the Raymond effect is at its strongest at the dome and weakens considerably over one ice thickness as one moves away from the flow center. Along the ridges leaving the dome, the Raymond effect is still present and decreases with the ratio of the flow across and along the ridge. In the vicinity of the dome, horizontal strain rates vary strongly from uniaxial to biaxial. Large-scale effects, represented in our model as fluxes at boundaries, seem to be the primary controls on dome position and shape.

Citation: Gillet-Chaulet, F., and R. C. A. Hindmarsh (2011), Flow at ice-divide triple junctions: 1. Three-dimensional full-Stokes modeling, *J. Geophys. Res.*, *116*, F02023, doi:10.1029/2009JF001611.

1. Introduction

[2] This paper presents the first three-dimensional finite element full system modeling of flow at nonaxisymmetric ice domes. Full system modeling of ice divides experiencing plane flow [*Raymond*, 1983; *Hvidberg*, 1996; *Pettit and Waddington*, 2003; *Martín et al.*, 2006, 2009a, 2009b] is now routine, and axisymmetric flows have also been considered [*Hvidberg*, 1996]. However, ice domes are rarely perfectly elongated or axisymmetric, and often it seems that they are the meeting points of three ice divide ridges or triple junctions, and in such areas three-dimensional effects cannot be neglected. Some topographic data and satellite imagery are used to present this assertion in a companion paper [*Hindmarsh et al.*, 2011, hereinafter Part 2]. A further example we use in this paper is the topography of the Greenland Ice Sheet in the summit area from a 5 km grid digital elevation model (DEM) [*Bamber et al.*, 2001], given in Figure 1. In this example, the dome is the meeting point of two well-defined ridges subtending an angle of 134°. At an equal angle between this two ridges, we can discern a weak third ridge. We will show in this paper that it shares many similarities with an ideal triple junction (i.e., where the dome is the meeting point of three identical ridges), and thus belongs to the family of the triple junctions.

[3] The wider significance of this observation relates to the fact that two ice cores, Greenland Ice Core Project (GRIP) and Greenland Ice Sheet Project 2 (GISP2) ice cores, were drilled in this area in the 1990s [*Hvidberg et al.*, 1997]. Ice domes are preferred sites for ice core drilling, both in Antarctica (e.g., Dome C [*EPICA Community Members*, 2004], Dome F [*Dome-F Deep Coring Group*, 1998], Berkner Island [*Mulvaney et al.*, 2007]) and in Greenland (Greenland Ice Core Project (GRIP) [*Dansgaard et al.*, 1993]), principally because the local provenance of the ice seems more assured. A further motivation is that vertical compression dominates under a dome center, giving a greatest chance of recovering an undisturbed stratigraphy.

[4] Because absolute dating techniques are usually not available, the dating of the cores relies strongly on ice-flow modeling, and since the problem is essentially one of inverse nature, one-dimensional flow models are still the only ones that are computationally practicable to use for dating dome cores [*Parrenin et al.*, 2007]. The longitudinal components of stresses and strain rates dominate compared with the shear components in ice domes and ridges areas. For this reason,

[1]Physical Sciences Division, British Antarctic Survey, Natural Environment Research Council, Cambridge, UK.

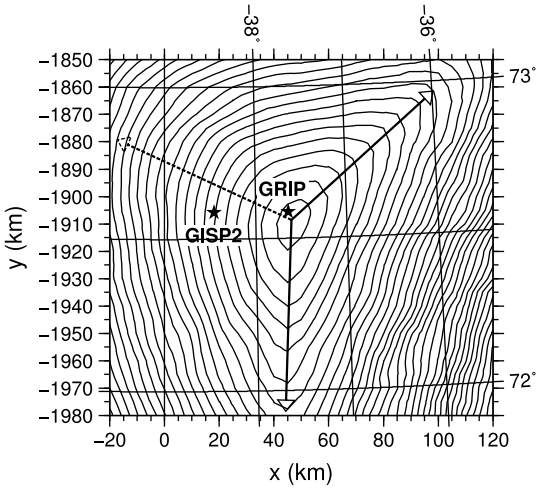

Figure 1. Five meter surface contours in the Greenland Ice Sheet summit area from a 5 km grid digital elevation model (DEM) [*Bamber et al.*, 2001]. Starting from the dome, two ridges are well defined. Estimates of their direction are plotted (solid arrows). The angle between these two estimates is 134°. The estimated direction of the weak third ridge (dashed arrow) is plotted at an equal angle between the two sharp ridges.

the Shallow Ice Approximation (SIA) [*Hutter*, 1983], widely used in large-scale ice flow models [e.g., *Ritz et al.*, 2001], does not hold in the vicinity of domes or ridges, and in consequence the full-Stokes equations must be used. Underneath a dome, owing to the vanishing of deviatoric stresses with depth, the nonlinear Glen rheology implies a highly viscous ice area and strong horizontal variations in the vertical strain rate. This effect was firstly described by *Raymond* [1983], and is now referred to as the *Raymond effect*. An obvious consequence is that the vertical velocity profile differs under the dome compared with the flank. As a consequence of this difference, *Raymond* [1983] predicted that isochrones would exhibit anticlines just under domes. Such anticlines were later discovered on radargrams [*Nereson et al.*, 1998b; *Vaughan et al.*, 1999] and are now called *Raymond arches*.

[5] Owing to the evident relationship between isochronal layers and the (past and present) velocity field [*Parrenin and Hindmarsh*, 2007], measured isochronal layers are now widely used to infer information about ice flow. In particular, the Raymond effect gives valuable information about ice rheology. Since the vertical velocity profiles under the dome and at the flank depend on the ice rheology [*Parrenin and Hindmarsh*, 2007; *Pettit and Waddington*, 2003], Raymond arches have been used to infer the constitutive relationship of ice and especially the value of the Glen index [*Martín et al.*, 2006]. Recently, theoretical studies have shown that anisotropy of ice may increase the size of the Raymond arches [*Pettit et al.*, 2007; *Martín et al.*, 2009a], as does a more nonlinear ice rheology.

[6] Since Raymond arches are also a consequence of the history of the ice flow, they have also widely been used for inferring ice geometry history [*Nereson et al.*, 1998b; *Nereson and Raymond*, 2001; *Price et al.*, 2007; *Martín et al.*, 2009b], accumulation pattern [*Nereson et al.*, 2000; *Martín et al.*, 2006], basal sliding and along ridge flow [*Pettit et al.*, 2007; *Martín et al.*, 2009b]. One may also note that the fact that ice divide ridges are clearly viewable in remote-sensed images is a consequence of their high curvature, which is itself a consequence of the nonlinear rheology of ice [*Fowler*, 1992; *Hindmarsh*, 1996; *Pettit and Waddington*, 2003].

[7] The occurrence of Raymond arches in the central part of ice sheets is still a matter of debate [*Jacobel and Hodge*, 1995] as low values of the Glen index, less than 2 and possibly close to 1, have been reported for these areas [*Doake and Wolff*, 1985; *Lliboutry and Duval*, 1985; *Lipenkov et al.*, 1997]. Another explanation for missing Raymond arches is that domes and ridges positions in large ice sheets are highly dependent on margin position and that they have not been in their actual position long enough for Raymond arches to form [*Anandakrishnan et al.*, 1994; *Hindmarsh*, 1996; *Marshall and Cuffey*, 2000]. The highly nonlinear (and thus non-SIA) vertical velocity profiles which have been used for the dating of the Dome C and Dome F cores [*Parrenin et al.*, 2007] give support to this explanation and suggest the occurrence of the Raymond effect, although this may also be related to the basal topography.

[8] Increases in computing power now mean that it is computationally feasible to model transient ice sheet and glacier flows in three dimension, solving the full-Stokes equations [*Le Meur et al.*, 2004; *Zwinger et al.*, 2007] coupled with the evolution of the upper free surface [*Pattyn*, 2008].

[9] Our scientific aim is, starting from an initially axisymmetric dome, to explore the formation of triple junctions. We want to explore the characteristic features of the topography and of the flow of ice, especially the Raymond effect, in the vicinity of triple junctions. We start with the working hypothesis that nonaxisymmetry of the dome is a consequence of nonaxisymmetry of the distal forcing. This automatically creates a number of ridges which can enter the dome area. A second hypothesis is that, with an appropriate symmetry in the distal forcing, more than three ridges could meet at a dome. We suppose that it is possible but extremely unlikely for a real ice sheet, and that this does not need to be modeled as the slightest perturbation will create two neighboring triple junctions. This argument has previously been developed by *Nye* [1991] in a catastrophe theory context of genericity and nongenericity.

[10] The situation where three divide ridges of equal strength meet at triple junction (an example from the Fletcher Promontory is shown in Part 2) is an instructive ideal, and we explore this. This situation implies a distal forcing with a threefold symmetry. We then consider distal forcing without such a threefold symmetry, varying both the geometry (angle subtended by forcing maxima) and the amplitude of the maxima. By doing this, we want to show that the case where the dome is the meeting point of two well-defined ridges and a weak (eventually vanishing) third ridge is a special type of triple junction. This would support the working hypothesis that triple junction exist at most domes.

[11] Specifically, we have two objectives: (1) use a full Stokes model to model triple junctions for a nonlinear rheology and (2) investigate the effects of nonthreefold symmetric forcing on triple junctions. The paper plan is to present the model, and investigate triple junction behavior under a number of different distal forcing scenarios. In the companion

paper [*Hindmarsh et al.*, 2011], we use these results to analyze observations from Thyssenhöhe, Berkner Island, and the Fletcher Promontory triple junctions, both located in West Antarctica.

2. The Model and Governing Equations

[12] We restrict our study to the flow of incompressible ice in a semicircular domain of radius R in the horizontal (x, y) space, where the $y = 0$ plane, aligned with the diameter of the domain, is a symmetry plane. This hypothesis is used to reduce our domain size as 3-D transient simulations are computationally expensive, but will allow us to model the case of an ideal triple junction resembling Fletcher Promontory, as well as the case of triple junctions with two sharp similar ridges and one weak ridge resembling Thyssenhöhe and the summit of the Greenland Ice Sheet.

2.1. Field Equations

[13] We use the finite element code ELMER [e.g., *Gagliardini and Zwinger*, 2008; *Gillet-Chaulet et al.*, 2006] to solve the full-Stokes equations for incompressible ice

$$\begin{cases} \nabla \cdot \boldsymbol{u} = 0 \\ \nabla \cdot \boldsymbol{\sigma} + \rho_i \boldsymbol{g} = 0 \end{cases}, \tag{1}$$

where $\boldsymbol{u} = (u, v, w)$ is the velocity vector, $\boldsymbol{\sigma}$ is the stress tensor, $\boldsymbol{g}$ is the acceleration due to gravity and ρ_i is the uniform density of ice. We use an isotropic Glen [*Glen*, 1955] constitutive relation for the ice flow law:

$$\tau = 2\eta e^{1/n-1}\boldsymbol{e}, \tag{2}$$

where $\boldsymbol{\tau}$ is the deviatoric stress tensor and $\boldsymbol{e}$ is the traceless strain rate tensor. The apparent (nonlinear) viscosity $\nu = \eta e^{1/n-1}$ is function of the intrinsic ice consistency coefficient η, of the second invariant of the strain rate tensor defined by $e^2 = 2\boldsymbol{e}{:}\boldsymbol{e}$, where we use the double contracted tensorial product ":", and of the Glen index n (set equal to 3, if not mentioned explicitly in the text).

[14] In the following, we model isothermal flow, so that η is uniform in space, except for one experiment in section 4.2.4 where we prescribe η to represent the influence of softer ice at higher temperatures near the bed. The ice is always supposed to be below the melting temperature, so no sliding is considered.

[15] The upper free surface $z = s(x, y, t)$ evolves according to the kinematical condition

$$\partial_t s + \boldsymbol{u}_H \cdot \nabla s = w + a, \tag{3}$$

where $\boldsymbol{u}_H = (u, v)$ is the surface horizontal velocity vector aligned with (x, y) the ice accumulation rate is denoted by a and is constant through time and space.

[16] The Stokes equations (1) and free-surface equation (3) are solved in a coupled way using a transient scheme until a (near) steady state is achieved. The criterion for steady state is that the maximum rate of displacement of a node on the free surface is less than 1 mm/yr. Small perturbation theory shows that the free surface in the divide area can evolve rapidly with respect to divide characteristic time s/a [*Nereson et al.*, 1998a] in response to changes in the boundary forcings. In our experiments the ice volume is kept constant through time so that the steady state topography is close to the initial topography, that is, the maximal change in ice thickness is of the order of a few percent. In consequence, the steady state as defined above is usually achieved after few percents of the ice divide characteristic time.

[17] When a steady solution for the surface elevation and the velocity is reached, the steady state age χ corresponding to the steady configuration, is calculated using

$$\boldsymbol{u} \cdot \nabla \chi = 1. \tag{4}$$

The age is zero on the upper free surface and we never consider situations of net melting here.

2.2. Boundary Conditions

[18] On the lower boundary, the ice is fixed to the immobile substrate, where

$$u = v = w = 0. \tag{5}$$

The upper surface is a stress free surface

$$\boldsymbol{\sigma} \cdot \mathbf{n} = 0, \tag{6}$$

where $\mathbf{n}$ is the unit vector pointing outward of the free surface. On the $y = 0$ plane, aligned with the diameter of the semicircular domain, symmetry conditions are applied

$$\begin{cases} v = 0 \\ \sigma_{xy} = \sigma_{yz} = 0. \end{cases} \tag{7}$$

[19] The circumference is not a physical boundary; it is used to reduce our domain size. As is common in plane-flow applications [e.g., *Raymond*, 1983; *Mangeney et al.*, 1996; *Hvidberg*, 1996; *Pettit and Waddington*, 2003], SIA assumptions are used to prescribe the conditions at this boundary. A horizontal velocity $\boldsymbol{u}_H$ and a vertical force are prescribed on the circumference.

[20] 1. We assume that the orientation of the horizontal velocity vector $\boldsymbol{u}_H$ is colinear with the surface slope vector and pointing in the opposite direction.

[21] 2. We assume that the norm $\|\boldsymbol{u}_H\|$ of the horizontal velocity vector varies with depth to the power $n + 1$ and is equal to zero at the bed at $z = 0$:

$$\|\boldsymbol{u}_H\| = K \times \left((s)^{n+1} - (s - z)^{n+1}\right), \tag{8}$$

where the constant K is a function of the surface slope, the ice stiffness, and the product of gravitational acceleration and density. In our simulations, to reach a steady state, the total volume of ice is kept constant through time by specifying that the ice flux entering through the free surface as accumulation $\pi R^2 a/2$ is equal to the ice flux leaving through the circumference

$$\int_0^{\pi} \int_0^{H} \boldsymbol{u}_H \cdot \mathbf{n}_c R \mathrm{d}z \mathrm{d}\theta = \frac{1}{2}\pi R^2 a, \tag{9}$$

where $\mathbf{n}_c = (\cos(\theta), \sin(\theta), 0)$ is the unit vector on the circumference pointing outward from the domain with $\theta = \arctan$

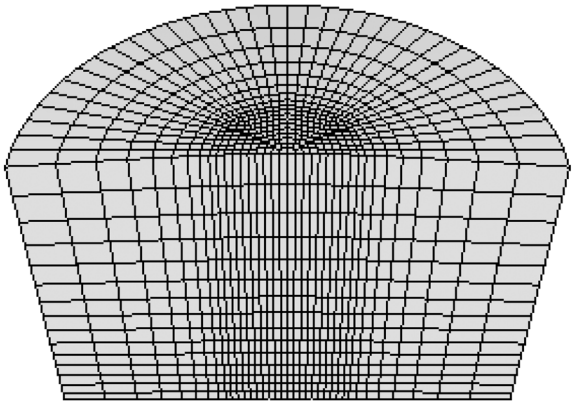

Figure 2. Three-dimensional view of the finite element mesh with a 30 times vertical exaggeration. The radius R of the domain is $15s_0$ or $20s_0$ (see Table 1).

(y/x). Using relation (9) we can determine the constant term K in equation (8) to obtain

$$\boldsymbol{u}_H \cdot \mathbf{n}_c = \frac{1}{2}\frac{n+2}{n+1}(s)^{-(n+2)} Ra\left[(s)^{n+1} - (s-z)^{n+1}\right] f(\theta), \quad (10)$$

where f is a function of θ that obeys the constraint

$$\int_0^{\pi} f(\theta)\mathrm{d}\theta = \pi. \quad (11)$$

Having $f(\theta) = 1$ leads to an axisymmetric boundary condition for the velocity, whereas a value of f greater than unity increases the outflow and a value of f lower than unity decreases the outflow.

[22] 3. As the vertical component of the velocity vector is left free, we apply the SIA shear stress profile

$$\boldsymbol{\sigma} \cdot \mathbf{n}_c \cdot \boldsymbol{e}_3 = \rho g \frac{\partial h}{\partial \mathbf{n}_c}(z-s). \quad (12)$$

[23] It is known that, when applying the shallow ice approximation at a boundary, the error induced by these nonphysical boundary propagates into the domain over few times the ice thickness. In two-dimensional calculations, the availability of computational power permits to place the boundary sufficiently far from the center of the domain and to exclude it from displays [*Raymond*, 1983; *Hvidberg*, 1996; *Martín et al.*, 2006]. This circumstance is not always possible with our three-dimensional calculations. However, the radius of our modeled domain is chosen to be larger than ten ice thicknesses so that the flow in the vicinity of the domain center is insensitive to the details of the boundary condition.

3. Experimental Design

3.1. Initial Conditions

[24] We prescribe the initial surface elevation to be axisymmetric. It is given by the analytical surface elevation obtained with the SIA at order zero of an isothermal ice sheet flowing over a flat bedrock [*Vialov*, 1958]:

$$s(r) = s_0\left(1 - \left(\frac{\epsilon}{s_0}r\right)^{(n+1)/n}\right)^{n/(2n+2)}, \quad (13)$$

where $r = \sqrt{x^2 + y^2} \in [0, R]$, s_0 is the prescribed initial dome elevation, and ϵ is a small parameter corresponding the ratio of the ice sheet dome elevation to the ice sheet extent.

[25] According to the SIA with constant and uniform accumulation a in (3) and ice consistency η in (2), the small parameter ϵ is given by

$$\epsilon^{(n+1)/n} = \left(\frac{n+2}{2}\right)^{1/n} \frac{2\eta}{\rho_i g s_0}\left(\frac{a}{s_0}\right)^{\frac{1}{n}}, \quad (14)$$

The experiments are repeated for a range of initial geometries given by equation (13) with $n = 3$. As, in our experiments, the ice volume is kept constant through time, for given initial volume and domain radius, the steady state should be independent of the detailed initial surface elevation. In general, a change in the initial geometry correspond also in a change of the model parameters η and a, and this is explicated in the main text. To reduce the computation time to reach a steady state, η and a are chosen from equations (13) and (14) so that the initial state of the ice sheet is close to the steady state obtained from the finite element calculation in the axisymmetric case.

[26] The finite element mesh that we used contains 7290 trilinear brick elements, leading to a total of 8369 nodes. The vertical direction is discretized by 15 layers. The uppermost layer is 2.5 times thicker than the lowermost layer. In the horizontal directions, the mesh is thinner in the central part. A 3-D view of the finite element mesh is shown in Figure 2.

[27] In one experiment, in section 4.2.4, we introduce a vertical variation in the temperature profile, written as a function of the normalized depth $\hat{z} = z/s$. This was based on a polynomial fit of the GRIP measured temperature [*Gundestrup et al.*, 1993] and was imposed over the whole domain [see *Gagliardini and Meyssonnier*, 2000]. The temperature is −32°C at the surface, nearly constant in the upper half part and then increases to −8.5°C at the bed. The ice fluidity $A_i = \eta^{-n}$ in (2) depends on the temperature through an Arrhenius relationship

$$A_i(T) = A_i^{T_0} e^{\frac{Q}{R}\left(\frac{1}{T_0} - \frac{1}{T}\right)}, \quad (15)$$

where $A_i^{T_0}$ is a reference ice fluidity at temperature T_0, $R = 8.314$ J mol^{-1} K^{-1} is the gas constant and $Q = 78$ kJ mol^{-1} the activation energy [*Lliboutry and Duval*, 1985]. The reference ice fluidity $A_i^{T_0}$ has been chosen so that

$$\int_0^s A_i(z-s)^n \mathrm{d}z = \int_0^s A_i^{\mathrm{iso}}(z-s)^n \mathrm{d}z. \quad (16)$$

This implies, according to the SIA, that, for a given surface slope, the surface horizontal velocities are identical in the isothermal case and with the GRIP temperature profile.

3.2. Dimensionless Results

[28] All the results are given in dimensionless form represented by the circumflex symbol, using the initial dome elevation s_0 in (13) and the ice accumulation a in (3):

$$(\hat{x},\hat{y},\hat{z},\hat{s}) = \frac{1}{s_0}(x,y,z,s),$$
$$(\hat{t},\hat{\chi}) = \frac{a}{s_0}(t,\chi), \tag{17}$$
$$\hat{e}_{ij} = \frac{s_0}{a}e_{ij}.$$

For the slope, a scale analysis by *Martín et al.* [2009b], related to a previous analysis by *Wilchinsky and Chugunov* [1997], shows that the slope γ_x is usefully scaled by a dimensionless parameter $\Lambda \ll 1$, which represents the slope magnitude at a distance on the order of one ice sheet thickness away from the divide:

$$\gamma_x \equiv \partial_x s(x/H=1) \sim \Lambda \equiv \frac{2\eta}{\rho_i g H}\left(\frac{a}{H}\right)^{\frac{1}{n}} \ll 1. \tag{18}$$

The quantities on the right hand side represent typical values at the divide when the ice is in steady state; values for Λ lie typically between 0.001 (thick ice, low accumulation rate) and 0.02 (thin ice, high accumulation). *Martín et al.* [2009b] showed that for ridges where the y slope (along-ridge slope) γ_y is nonzero, the flow may be parameterized by the slope ratio $\delta = \gamma_y/\Lambda$.When δ is small, the momentum balance equations in the x and y directions partially uncouple, meaning that the problem can be solved in the 2-D (x, z) plane. Furthermore, as those authors showed, the amplitude of steady Raymond arches depends strongly on the along-ridge slope as expressed by the parameter δ; We use the same scaling in this work and the surface slope γ scaled by Λ (18) is denoted by

$$\hat{\gamma} = \frac{1}{\Lambda}\gamma. \tag{19}$$

3.3. Experiment A: Axisymmetry

[29] These experiments assess the influence of the mesh on the results and the stability of the 3-D model. The model is run with an axisymmetric boundary condition on the circumference, that is, $f(\theta) = 1$, until it reaches a steady state. Results are compared with the results obtained with a much higher-resolution two-dimensional axisymmetric model based on the same assumptions. For this 2-D axisymmetric model the mesh is composed of 2700 bilinear quadrilateral elements for a total of 2806 nodes. The vertical direction is discretized by 45 layers, with the uppermost layer 3 times thicker than the lowermost layer. Along the x direction, the size of the elements is 10 times larger near the circumference than near the dome, so that, in the vicinity of the dome, the horizontal dimension of the elements is approximately 6 times smaller in the 2-D axisymmetric model than in the 3-D model.

3.4. Experiment B: Threefold Symmetry

[30] We now seek to describe and understand the flow of ice in a triple junction with a threefold symmetry. Such a symmetry in the ice flow is created by imposing a threefold symmetry on the boundary forcing, so $f(\theta)$ is chosen as piecewise linear function as

$$f(\theta) = \begin{pmatrix} 1 - F + 2F \times 3\theta/\pi & \text{for } \theta \le \pi/3 \\ 1 + F - 2F \times 3(\theta - \pi/3)/\pi & \text{for } \pi/3 < \theta \le 2\pi/3 \\ 1 - F + 2F \times 3(\theta - 2\pi/3)/\pi & \text{for } \theta > 2\pi/3 \end{pmatrix}, \tag{20}$$

where the outflow parameter $F \in [0, 1]$. Experiments are performed for different values of F and n.

3.5. Experiment C: Threefold Symmetry Broken by Nonuniform Angles

[31] We now explore breaking of the threefold symmetry by altering the entry angle of the boundary forcing that produces the divide ridges. For this experiment the minimum and maximum values of $f(\theta)$ are the same as for Experiment B, but the maxima are for $\theta = 0°$ and $\theta = 105°$. Hence, $f(\theta)$ is chosen as

$$f(\theta) = \begin{pmatrix} 0 + 2 \times 24\theta/7\pi & \text{for } \theta \le 7\pi/24 \\ 2 - 2 \times 24(\theta - 7\pi/24)/7\pi & \text{for } 7\pi/24 < \theta \le 7\pi/12 \\ 0 + 2 \times 12(\theta - 7\pi/12)/5\pi & \text{for } 7\pi/12 > \theta \end{pmatrix}. \tag{21}$$

3.6. Experiment D: Threefold Symmetry Broken With Unequal Forcing Amplitude

[32] In these experiments we explore the effects of symmetry breaking by altering the amplitude of forcing of the divide ridges at the boundaries. The maxima of $f(\theta)$ are at $\theta = 0°$ and $\theta = 120°$ but the values of the maxima are different, $f(\theta)$ is chosen as

$$f(\theta) = \begin{pmatrix} 0.7 + 0.6 \times 3\theta/\pi & \text{for } \theta \le \pi/3 \\ 1.3 - 1.25 \times 3(\theta - \pi/3)/\pi & \text{for } \pi/3 < \theta \le 2\pi/3 \\ 0.05 + 2.55 \times 3(\theta - 2\pi/3)/\pi & \text{for } \theta > 2\pi/3 \end{pmatrix}. \tag{22}$$

4. Results

[33] All the experiments are denoted by a letter representing the type of forcing presented in sections 3.2–3.6 (A, B, C, or D) and a number representing the initial surface elevation (1–4); see Table 1 and equation (13).

4.1. Experiment A

[34] In order to compare the accuracy of the two and three dimensional solutions, the surfaces, scaled slopes and surface longitudinal strain rates obtained with the 2-D axisymmetric model and along the x axis of the 3-D model for experiment A1 are plotted in Figure 3. The solutions given by the two models are nearly identical, showing the ability of our 3-D

Table 1. Values of Parameters Defining Initial Domain Geometries[a]

Initial Geometry	s_0 (m)	ϵ	R
1	3000	10^{-2}	$20s_0$
2	3000	6.2×10^{-3}	$20s_0$
3	2000	2×10^{-2}	$20s_0$
4	1000	4×10^{-2}	$15s_0$

[a]Dome elevation, s_0; mean slope, ϵ; and radius, R, of the modeled domain.

model to capture the main features of the Raymond effect even with a mesh that is much coarser than the meshes that are practical in 2-D experiments. We are confident that a refined mesh would not increase the accuracy of the surface results given by the 3-D model. The results obtained here reproduce the main features from previous higher-resolution 2-D models of the Raymond effect [*Pettit and Waddington*, 2003; *Martín et al.*, 2006]. The consequences of an operating Raymond effect on the surface topography, the strain rate pattern and the isochrones are briefly reprised here. In describing the results of the experiments, we think of the divide as a starting point from which we move out.

[35] In the dome area, there is a very high gradient in the slope over a distance of approximately one ice thickness. Further away, the absolute value of the slope increases continuously and nearly linearly with distance from the dome. The Raymond effect produces a relatively high surface vertical strain rate under the dome, and a smaller and nearly uniform value at distances greater than two ice thicknesses from the divide, with a steep gradient over those two ice thicknesses. Continuity requires that surface horizontal strain rates are also large in magnitude in the vicinity of the dome where the vertical strain rates are large. The strain rate state is axisymmetric, that is, $\hat{e}_{xx} = \hat{e}_{yy}$, just under the dome at $x = 0$, but $\hat{e}_{xx} < \hat{e}_{yy}$ for $0 < \hat{x} < 5$. For $\hat{x} \geq 5$ the two strain rates are nearly constant and equal.

[36] The steady state isochrones obtained with the two models are plotted in Figure 3d. The Raymond effect leads to the formation of the so-called Raymond arches, that is, convexities in the isochrones, whose amplitudes are defined as the difference in elevation between the apex of the isochrone and its elevation in the flow area away from the divide. For the upper half part of the ice sheet the isochrones computed with the two models are nearly identical. In the lower half part, with the 3-D model, the highest point of the arches is underestimated, and away from the dome the lowest isochrones are a little deeper compared with the 2-D model. In summary, the 3-D model underestimates by a little the arch amplitude in the lower part of the ice sheet.

4.2. Experiment B

4.2.1. Effect of Boundary Forcing Amplitude F

[37] To allow visual comparison of the effect of F, the steady free surfaces obtained for experiment B1 with $F = 0.5$ and $F = 1$ in equation (20) are plotted in Figure 4. On this plot are also shown the dimensionless surface vertical strain rate $\hat{e}_{zz}$ and the surface horizontal velocity vectors on the circumference. All the other parameters of the model are kept constant in these experiments.

[38] The threefold symmetry forcing produces an ideal triple junction. In the modeled domain, two ridges of equal strength are present at 0° and 120°, at which point the outflow at the boundary is the smallest. The ridges show more curvature, that is, the ratio δ of the slope along the ridge over the slope parameter Λ (see equation (18)) is smaller, as the outflow parameter F increases.

[39] The vertical strain rate on the surface is greatest under the dome where the Raymond effect is the highest. This effect also operates under the ridges; it is greater where the ridges are more defined and it decreases when the slope ratio δ increase. The effect of varying the boundary forcing F on the surface elevations $\hat{s}$, the scaled slopes $\hat{\gamma}$ and the surface longitudinal strain rate components $\hat{e}_{ii}$ obtained along the diameter are shown in Figure 5a.

[40] There are small spurious oscillations on the surface and the slope at around $5s_o$ each side of the dome. Of course, the slope is a differentiated quantity and therefore more susceptible to noise. The oscillations coincide with the transition between the fine inner mesh and the coarser outer mesh. In

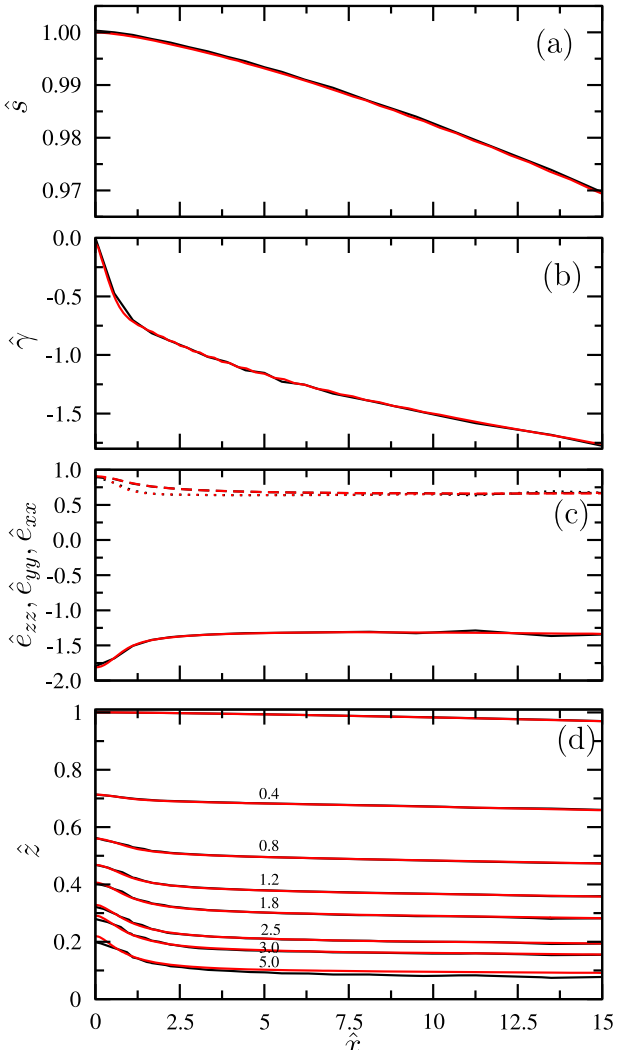

Figure 3. Experiment A1. Plots along the diameter $\hat{x}$ of (a) the surface $\hat{s}$; (b) the scaled slope $\hat{\gamma}$; (c) the surface longitudinal strain rates $\hat{e}_{xx}$ (dotted lines), $\hat{e}_{yy}$ (dashed lines), and $\hat{e}_{zz}$ (solid lines); and (d) several isochrones. Results obtained with the 3-D model are in black, with the 2-D axisymmetric model in red.

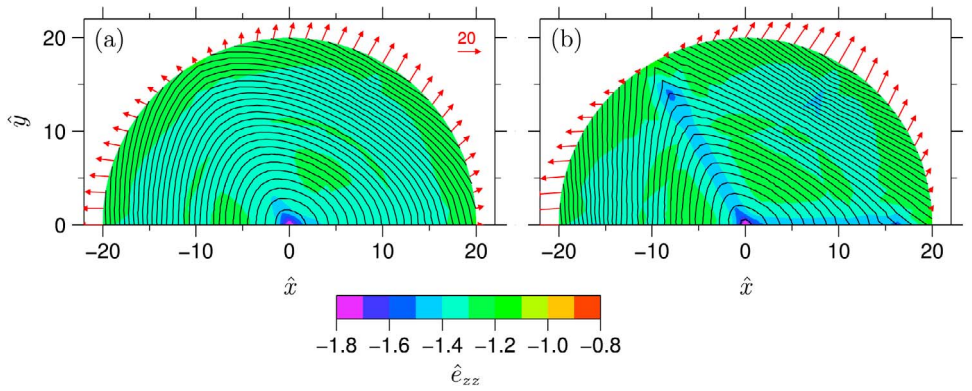

Figure 4. Experiment B1, the effect of boundary forcing amplitude F (equation (20)). Ice surface contours and surface vertical strain rate $\hat{e}_{zz}$ obtained for (a) $F = 0.5$ and (b) $F = 1$. Red arrows on boundary are the horizontal surface velocity vectors.

3-D, the mesh refinement is not an easy task especially with brick elements. But, we are confident that increases in computing power will permit these problems to be overcome, and the wiggles shown to be spurious features, and we are also confident that the overall pattern shown is correct.

[41] In the immediate vicinity of the dome, as observed in the axisymmetric case, the slope increases very quickly over a distance of approximately one ice thickness either along the ridge (right-hand side, $\hat{x} > 0$) and along the talweg (left-hand side of Figure 5a, $\hat{x} < 0$) (talweg is a geomorphological term meaning the line of the bottom of a valley). An important result is that, in this area, the slope pattern is independent of the value of F and thus can be used to quantify the Raymond effect under the dome independently of the strength of the ridges leaving the dome.

[42] Moving further away along the ridge, the scaled slope increases steadily in absolute value for the lower amplitude case $F = 0.5$, but reaches a stable value around −1 and decreases a little in absolute value near the boundary for $F = 1$. Moving further away along the talweg, the slope increases nearly linearly and increases more as F is bigger, but the difference between the two curves remains small.

[43] An interesting result that can be seen in the strain rate plot, is that just under the dome, ice experiences an axisymmetric vertical compression, that is, $\hat{e}_{xx} = \hat{e}_{yy} = -\hat{e}_{zz}/2$. But, there are large variations of the strain rate state in the immediate vicinity of the dome from a mainly xz plane deformation state (i.e., $\hat{e}_{xx} > \hat{e}_{yy}$) on the talweg (Figure 5a, left-hand side), to a yz plane deformation state (i.e., perpendicular to the ridge, $\hat{e}_{yy} > \hat{e}_{xx}$) on the ridge side (Figure 5a, right-hand side). The ratio between the two strain rates along the horizontal directions $\hat{e}_{xx}$ and $\hat{e}_{yy}$ is larger as the ridge is sharper, that is, as F is higher. Owing to the Raymond effect, the vertical strain rate shows a higher absolute value just under

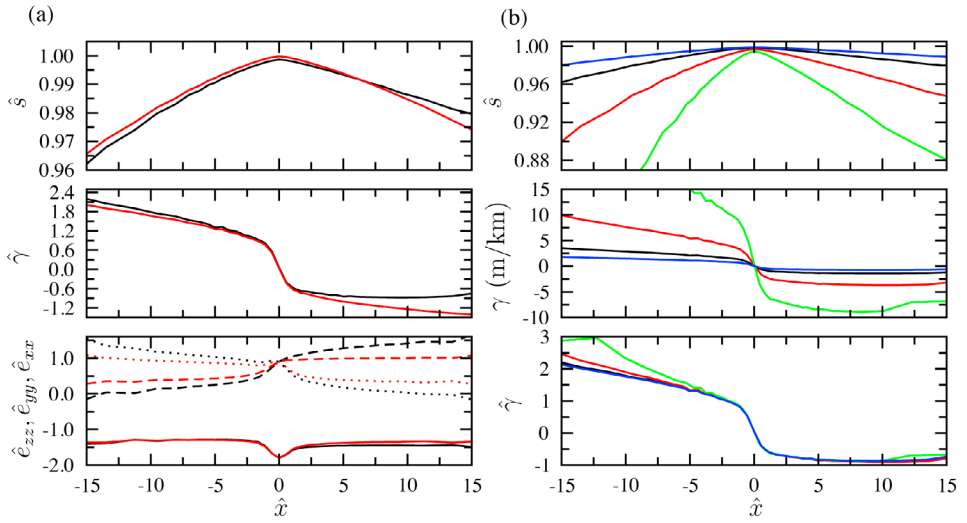

Figure 5. (a) Experiment B1, the effect of boundary forcing amplitude F (equation (20)). Plots are along the diameter $\hat{x}$ of surface $\hat{s}$; scaled slope $\hat{\gamma}$; and surface longitudinal strain rates $\hat{e}_{xx}$ (dotted lines), $\hat{e}_{yy}$ (dashed lines), and $\hat{e}_{zz}$ (solid lines). Results obtained with $F = 1$ in black and $F = 0.5$ in red. (b) Experiments B1–B4, the effect of initial volume and accumulation. Plots along the diameter $\hat{x}$ of surface $\hat{s}$, slope γ, and scaled slope $\hat{\gamma}$ for initial condition 1 (black), initial condition 2 (blue), initial condition 3 (red), and initial condition 4 (green) (Table 1).

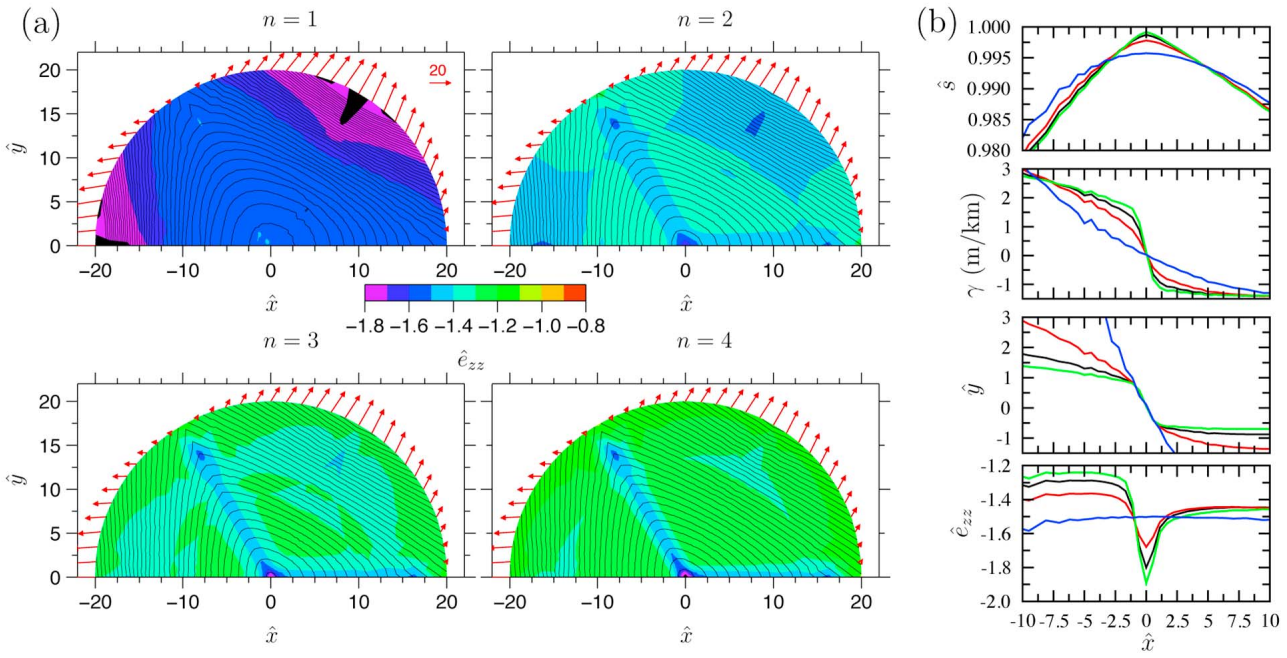

Figure 6. (a) Experiment B1, the effect of Glen index n. Ice elevation contours and surface vertical strain rate $\hat{e}_{zz}$ for $n = 1$, $n = 2$, $n = 3$, and $n = 4$. Surface velocity vectors in red on the circumference. (b) Plots along the diameter $\hat{x}$ of surface $\hat{s}$, slope γ, scaled slope $\hat{\gamma}$, and surface vertical strain rate $\hat{e}_{zz}$ for $n = 1$ (blue), $n = 2$ (red), $n = 3$ (black), and $n = 4$ (green).

the dome and decreases quickly over a distance of less than two ice thicknesses as we move away from the dome. Under the ridge, on the right-hand side of Figure 5a, the Raymond effect operates, but is muted somewhat by the presence of an along-ridge slope, as predicted by *Martín et al.* [2009b]. In the remaining part of section 4.2 all the results are obtained with $F = 1$.

4.2.2. Effect of Initial Volume, Dome Elevation, and Accumulation

[44] In these experiments, we change the initial volume by changing the initial surface elevation as given in Table 1. This allow us to change two of the three parameters that enter the definition of the slope parameter Λ in equation (18): the dome elevation s_0 and the ice accumulation a. The ice consistency η is constant and uniform in all the experiments. The uniform and constant accumulation a is chosen from the analytical solution (14); between initial conditions 3 and 4, only the initial volume, and thus the dome elevation, changes and a is unchanged.

[45] In Figure 5b, we compare the variation of the surface elevation, the slope, and the scaled slope as a function of dimensionless position on the diameter. The greater the parameter ϵ, the greater the increase of slope as we move away from the dome. However, when scaled by Λ, the variation of slope $\hat{\gamma}$ with dimensionless distance is identical for all the experiments in the vicinity of the dome, that is, over a distance of approximately two ice thicknesses. Along the ridge (Figure 5b, right-hand side), all the results show the same variation. Along the talweg, away from the dome, the scaled slope $\hat{\gamma}$ increases more rapidly with distance from the flow center as ϵ increases, but this difference is small for the low values of ϵ. The oscillations obtained with initial condition 4, near the edges are assumed to be the consequence of the SIA profiles used for the boundary condition, as for this case the domain extended only 15 times the ice thickness from the initial dome center.

4.2.3. Effect of the Glen Index *n*

[46] Here we compare the results of the calculations that comprised experiment B1 with $n = 1$, $n = 2$, $n = 3$ and $n = 4$. The initial surface elevation and the constant accumulation a are the same for all the experiments. When $n \neq 3$, the ice consistency η is chosen so that the surface elevation according to the SIA in the axisymmetric case (equations (13) and (14)), would be equal to the initial surface elevation with $n = 3$ in $r = 0$ and $r = R$.

[47] Shown in Figure 6a are the steady surface profile, the surface vertical strain rate $\hat{e}_{zz}$ and surface horizontal velocity vectors on the circumference. For all four cases we obtain a stable ideal triple junction with ridges orientated at 120°. The ice surface ridges are sharper and more well defined as n increases. For $n = 1$, the surface contours in the vicinity of the dome are still nearly circular. As expected, the greater the value of n, the more marked is the Raymond effect, and the absolute value of the vertical strain rate $\hat{e}_{zz}$ just under the dome and the ridges also increases with n.

[48] The surface, the slope, the scaled slope and the surface vertical strain rate are plotted in Figure 6b. The variation of the slope is very different for $n = 1$ and $n > 1$. With $n > 1$ as discussed before, on both sides of the dome, there is a steep gradient of the slope over a distance of approximately one ice thickness; this gradient is steeper as n increases On the side of the ridge (right-hand side of Figure 6b), away from the dome, the slope increases in absolute value toward a stable value, and this value is reached over a shorter distance as n increases. Along the talweg (left-hand side of Figure 6b), the slope increases nearly linearly as we move away from the dome.

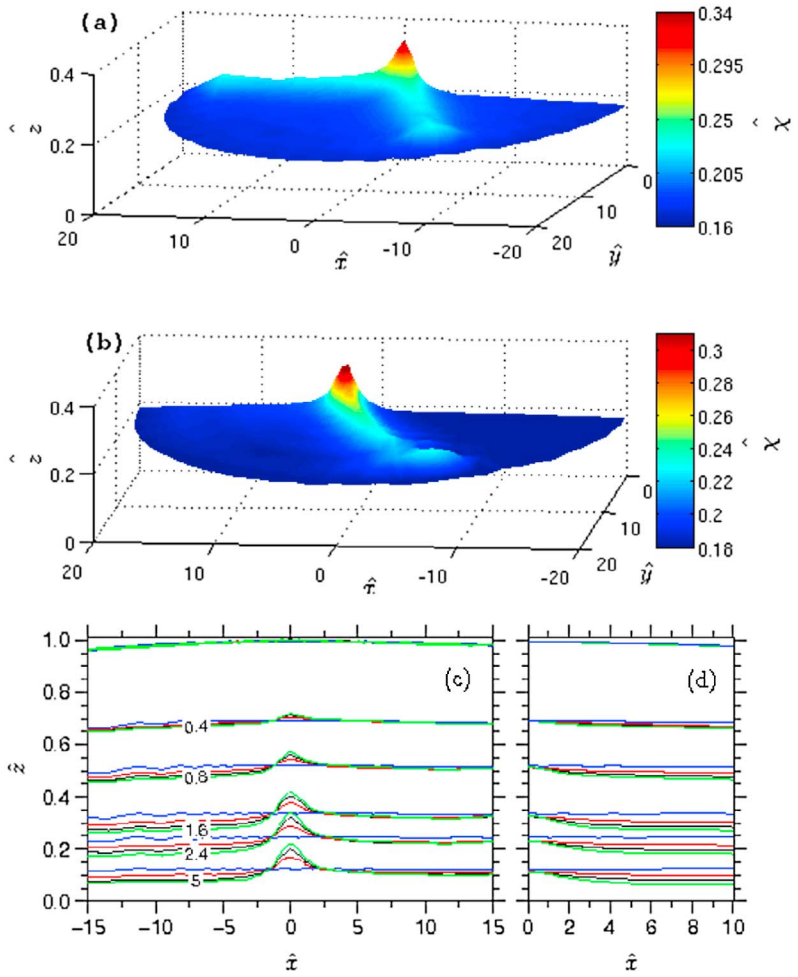

Figure 7. Experiment B1, the effect of n. (a) Three-dimensional view of isochrone corresponding to $\hat{\chi} = 2.4$ for $n = 4$; (b) isochronal layer for experiment D2 at $\hat{t} = 0.058$ (see Figure 10b). Isochrones are calculated for $n = 1$ (blue), $n = 2$ (red), $n = 3$ (black), and $n = 4$ (green) (c) in the symmetry plane and (d) perpendicular to the ridge at a distance $5s_0$ from the dome.

The increase in the slope is higher when n is greater. With $n = 1$, there is no abrupt variation of the slope in the vicinity of the dome, and the slope increases continuously on each side of the dome.

[49] The variation of the scaled slope in the vicinity of the dome is identical whatever the value of n. Under the ridge the absolute value of the scaled slope is smaller as n is higher, while along the talweg the increase of the scaled slope, as we move away from the dome is smaller as n is higher.

[50] We show a view of the three-dimensional isochrone surface in Figure 7a, demonstrating a strong central Raymond cupola, and Raymond bumps emanating along all three arms. In Figure 7c, we plot the steady state isochrones for different n on the reflection-symmetry plane $y = 0$. With $n = 1$, the isochrones are flat as expected (no Raymond bumps). For $n > 1$, in a pattern which reflects the surface vertical strain rate shown in Figure 6, the maximum height of the Raymond bumps is located just under the dome. This maximum height is higher as n is higher. The reflection-symmetry plane runs along a ridge on the right-hand side of Figure 7c, and the Raymond effect operates but is muted somewhat by the along-ridge slope. To the left of the dome, along the talweg, the isochrone apices deepen over a short distance since here the Raymond effect does not operate, and are also deeper at the same point as n increases. Along the ridge to the right of the dome the elevation of the isochrones is higher than to left.

[51] Figure 7d shows the isochrones for different n on a line perpendicular to the ridge at a distance $5s_0$ from the dome. As on the symmetry plane, a linear rheology for the ice leads to flat isochrones. For $n > 1$ the isochrones show small amplitude Raymond bumps. The highest points of the isochrones are located under the ridge and their ages were chosen to give the same elevation for all values of n, but away from the ridges, isochrones are deeper as n is higher leading to bigger Raymond bumps.

4.2.4. Effect of Nonuniform Temperature

[52] We have seen from the previous experiments that, for an ideal triple junction, the slope pattern in the immediate vicinity of the dome is only a function of the dimensionless parameter Λ (equation (18)) which depends on the Glen index, the ice thickness, the accumulation and the ice consistency. In real ice sheets, owing to the temperature gradient in the ice, the ice consistency can vary strongly from the upper surface to the bed, so that, in general, the choice of a typical

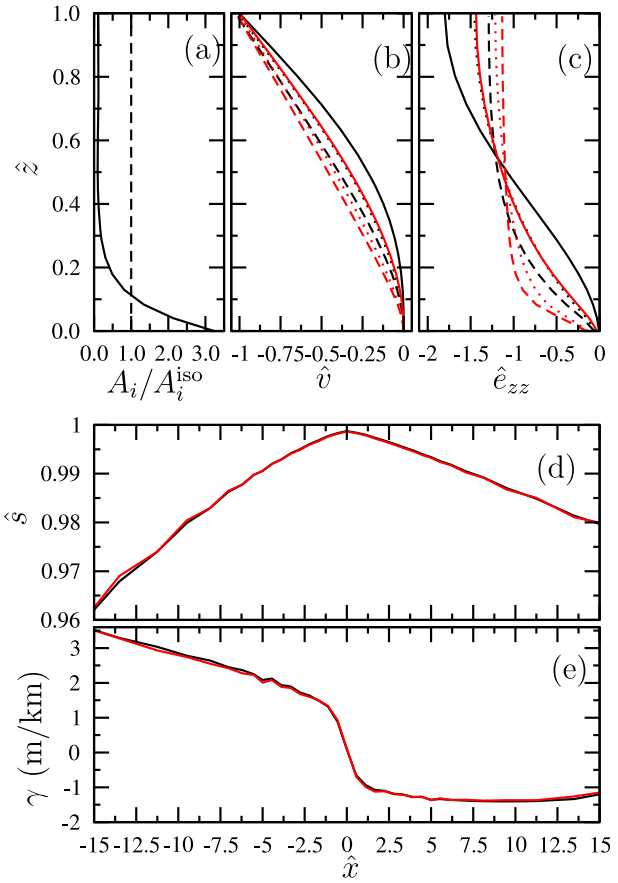

Figure 8. Experiment B1, the effect of temperature. (a) Fluidity relative to the isothermal fluidity as a function of reduced depth $\hat{z}$. The dashed line corresponds to the relative isothermal fluidity (i.e., equal to 1); (b) vertical velocity and (c) strain rate profiles under the dome (solid lines), at a distance $5s_0$ from the dome on the ridge side (dotted lines), and at a distance $5s_0$ from the dome on the opposite side (dashed lines). (d and e) Plots along the diameter $\hat{x}$ of the surface $\hat{s}$ and the slope γ. Results obtained in the isothermal case are in black, and results for the GRIP temperature profile case are in red.

value for η to calculate Λ is difficult. Specifically here, we use the GRIP temperature profile to see if it is possible to infer useful information about the ice flow law in Greenland from the dome topography presented in Figure 1. As described in section 3.1, the ice fluidity $A_i(T)$ varies with normalized depth (equations (15) and (16)), and is plotted in Figure 8a. According to the temperature profile, the fluidity is nearly constant and very low in the upper 70% of the ice sheet and then increases rapidly toward the bed. The intersection with the value of the fluidity used for the isothermal experiment A_i^{iso} is at 10% of the ice thickness above the bed.

[53] The GRIP temperature profile is not in a state of thermal equilibrium but still has memory of the last glacial maximum temperatures [*Gundestrup et al.*, 1993]. As said above, the free surface reacts very quickly to changes in the boundary forcing, so that our hypothesis is that the free surface can reach a quasi-steady state independently of the state of the temperature field, whether the temperature field is steady or unsteady. Specifically, we do not think that the "hot spot" patterns described by *Nereson and Waddington* [2002], associated with the operation of the Raymond effect, will play a role in the dynamical situations we are seeking to model. Finally, the choice of a vertically stretched temperature profile in our domain extending only 20 times the ice thickness in the horizontal direction, is justified by the small differences between the GRIP and GISP2 temperature profiles [*Gundestrup et al.*, 1993; *Clow et al.*, 1996].

[54] Vertical velocity and vertical strain rate profiles under the dome and at a distance $5s_0$ from the dome in the ridge side and at a corresponding position on the talweg side are plotted in Figures 8b and 8c. These profiles are different in absolute values, in the isothermal and GRIP temperature profile cases, but both show the same expected pattern: a highly nonlinear vertical velocity profile beneath the dome where the Raymond effect is at its maximum. Away from the dome, on the talweg side, the vertical velocity profile is more linear, especially in the upper part. The vertical velocity profile $5s_0$ from the dome in the ridge side is between the dome and the flank profiles as the Raymond effect still operates but is muted by the along-ridge flow. The vertical velocity profiles reflect these differences. With the GRIP temperature profile, the vertical velocity profile is less nonlinear under the dome and more linear in the flank compared with the isothermal case. Despite these differences in the vertical profiles, the surface and slope plotted along the diameter in Figures 8d and 8e are very close and present the same pattern discussed previously.

4.2.5. Discussion

[55] We have shown that a 120° periodic boundary condition for the ice flux leads to the formation of a stable ideal triple junction where the dome is the symmetric meeting point of three identical ridges.

[56] The surface slope along the ridge and the talweg depend on the ice flux on the boundary, and the smaller the flux along the ridge, the sharper the ridge. The Raymond effect is at its maximum under the dome and decreases quickly over few ice thicknesses, but is still operating under the ridges and, as demonstrated with a "2.5-D" model by *Martín et al.* [2009b], the smaller the along-ridge slope, the greater the Raymond effect.

[57] The surface slope shows large variations in the vicinity of the dome over a distance of one to two ice thicknesses, either along the ridge or along the talweg, but the variation is smaller on the ridge side. We have shown that, in the immediate dome vicinity, the slope scaled by Λ exhibits exactly the same gradient, and this depends neither on the ice fluxes on the boundary nor on vertical variations of the ice consistency with temperature. Thus, this gradient depends on the ice thickness, the accumulation rate, the ice consistency and the Glen index, allowing us to determine one of the variables if the others are known.

[58] As expected from previous results using 2-D modeling, the surface vertical strain rate varies highly in the vicinity of the dome and ridge, and this variation is higher as the Glen index n is higher. Moreover, we have shown that the strain rate state also changes over very short distances in the dome vicinity, from a mostly along-ridge plane deformation to a mostly plane deformation perpendicular to the ridge on the ridge side, with an axisymmetric compression just under the dome. As a consequence, the ice in the dome vicinity will experience very different strain rate states even with small

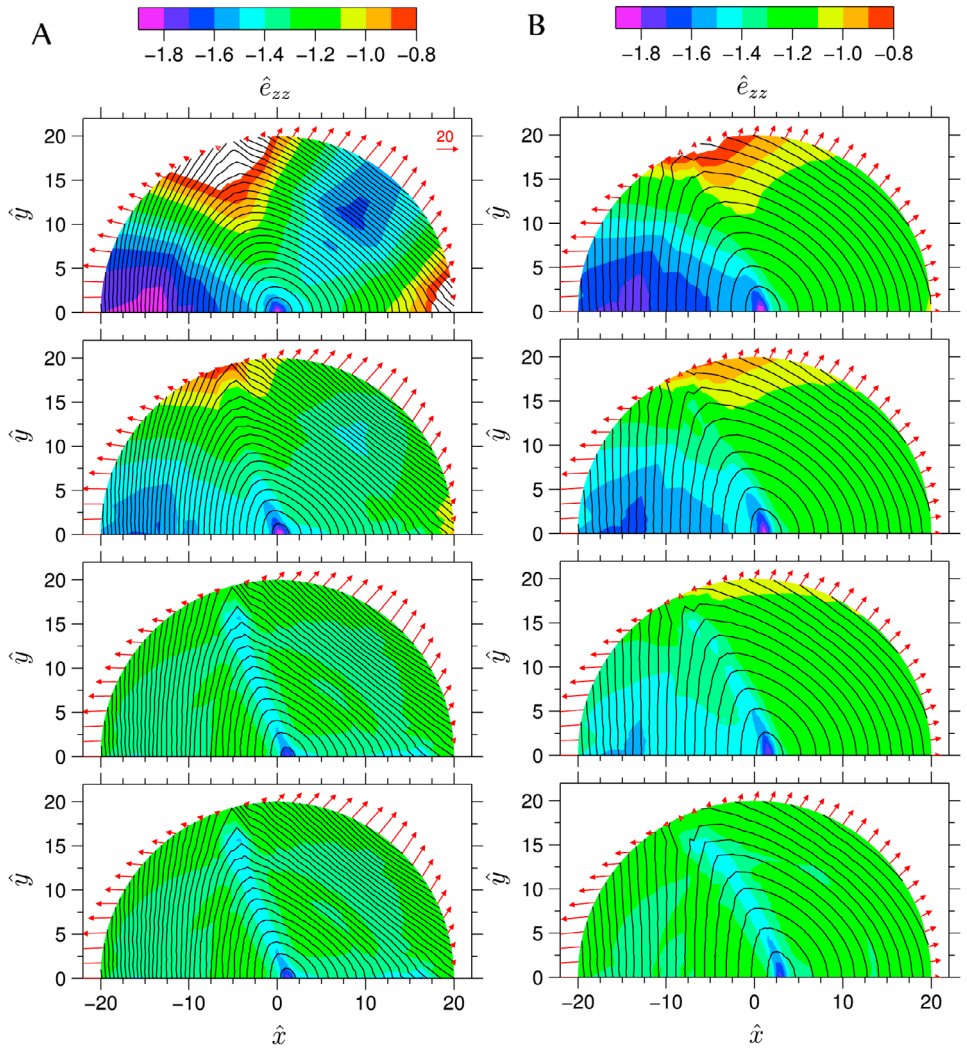

Figure 9. (a) Experiment C1. Surface contours and surface vertical strain rate $\hat{e}_{zz}$ obtained at (from top to bottom) $\hat{t} = 0.01$, $\hat{t} = 0.02$, $\hat{t} = 0.04$, and $\hat{t} = 0.24$. Horizontal surface velocity on the perimeter is shown by red vectors. (b) Experiment D2. Surface contours and surface vertical strain rate $\hat{e}_{zz}$ obtained at (from top to bottom) $\hat{t} = 8.7 \times 10^{-3}$, $\hat{t} = 0.012$, $\hat{t} = 0.017$, and $\hat{t} = 0.058$. Horizontal surface velocity on the perimeter is shown by red vectors.

peregrinations of the dome (i.e., of the order of one or two ice thicknesses). Such large changes have been suggested to be responsible for flow disturbances such as boudinage or folding especially in the presence of strongly anisotropic layers [*Dahl-Jensen et al.*, 1997; *Thorsteinsson and Waddington*, 2002; *Durand et al.*, 2007].

4.3. Experiment C

[59] In this experiment, the three fold symmetry is broken by nonuniform angles so that the central point, that is, the initial dome location, is no longer the center of a threefold symmetry. As a consequence the dome position migrates from its initial position to a new stable position, to form a nonsymmetric triple junction with two ridges (one in the modeled domain and its symmetric) sharper than the third ridge.

[60] We examine the development of the surface elevation and surface vertical strain rate $\hat{e}_{zz}$ through time in Figure 9a at four different times from experiment C1. At the beginning, two ridges start to develop, a straight ridge along the diameter on the right hand side and a curved ridge in the domain with an orientation varying from approximately 120° near the dome to 105° near the boundary. As time passes, this ridge becomes sharper and the dome starts to move toward a stable position, leading to a straighter ridge with an orientation of approximately 113°. This ridge is a little bit sharper than the one running along the diameter.

[61] We assume that the stable position of the dome is an equilibrium point with respect to the ice flux at the boundary, and thus depends only on the symmetries of our boundary conditions. But the transient process where the dome first forms a triple junction and then migrates with only minor changes to the topography in the dome vicinity is a noteworthy feature. The time involved for the initially axisymmetric dome to form a triple junction depends on the magnitude of the changes at the boundary but takes only a few

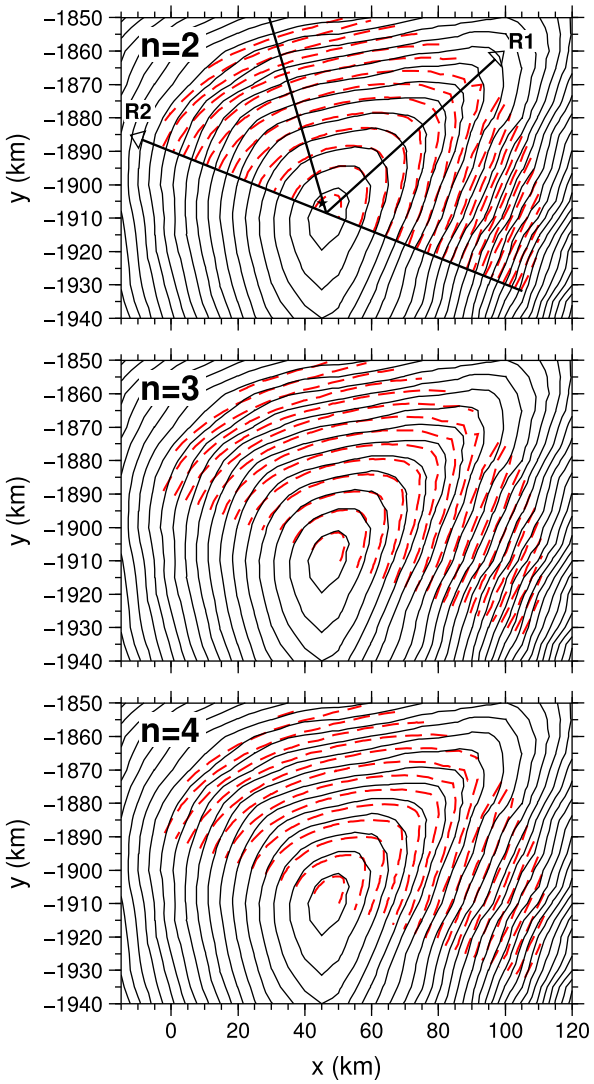

Figure 10. Experiment D2. Comparison of surface contour elevations (every 5 m) in the area of the GRIP ice core given by a 5 km grid DEM of Greenland [*Bamber et al.*, 2001] (black lines) with the surface elevation (red lines) obtained with (top) $n = 2$, (middle) $n = 3$, and (bottom) $n = 4$ at $\hat{t} = 0.017$. In Figure 10 (top) the star is the position of the GRIP ice core, and the lines R1 and R2 are estimates of the modeled divide locations.

percent of the divide characteristic time s/a (section 2.1) in our experiments, consistent with plane-flow perturbation analyses [*Hindmarsh*, 1997].

[62] For this nonsymmetric triple junction, it is interesting to notice that the strain rate state under the dome is not an uniaxial compression, and $e_{xx} > e_{yy}$. As for the ideal triple junctions in the previous experiments, the Raymond effect operates under the dome and the ridges, and increases as the ridge sharpens.

4.4. Experiment D

[63] In this experiment, the three fold symmetry is broken by changing the amplitude of the ice flux on the boundary. Again the initial dome location is no longer a threefold symmetry center, which causes the dome to migrate.

[64] In a similar way to experiment C, the surface elevation and surface vertical strain rate $\hat{e}_{zz}$ obtained at four different times of experiment D2 with $n = 3$ are plotted in Figure 9b. As in the previous experiment a curved ridge forms and the dome moves from its initial position to a stable position. Locally the dome is elongated transverse to the axis of symmetry, turning into a curved ridge. The ridge running along the diameter is very weak. The Raymond effect continues to operate under the dome and the stronger ridge, whereas the weaker ridge does not show higher vertical strain rates. At the beginning, the vertical strain rate is even higher in the talweg opposite to the weakest ridge (left-hand side) because the surface has not reached a stable position.

[65] We have shown above that surface topography was not influenced by a vertically varying temperature profile when compared with an isothermal simulation. The initial surface elevation of experiment D2 has the same characteristic ice thickness and slope as the GRIP area. We can then compare our modeled surface topography to the observed surface topography to infer the Glen index n in this area.

[66] The surface elevation in the GRIP area is compared with the surface elevations obtained at $\hat{t} = 0.017$ for $n = 2$, $n = 3$ and $n = 4$. For Summit this corresponds to approximately two centuries of evolution.

[67] Modeled surfaces are shifted vertically by +280 m to allow for the mean bed elevation at Summit, and their symmetries rotated so that the estimated modeled main ridge direction matches the northern ridge. This is ridge R1 in Figure 10. The ridge R2 in Figure 10 corresponds to the diameter of the modeled domain. For all the values of n, the modeled main ridge makes an angle of 64° with the diameter, so that the difference between the ridge R2 and the estimated weak ridge in Figure 1 is 3°.

[68] The modeled surface contours are very close to the real surface contours, so that the main characteristics of the Greenland Summit triple junction are well reproduced by our 3-D model. However, the differences in the surface contours for the three values of n are small especially in the dome vicinity. The differences are more visible on the surface slopes along the ridges R1 and R2, shown in Figure 11. As shown in experiment A, the greater the value of n, the higher the gradient of the slope in the dome vicinity, and the smaller the increase of the slope along the talweg as we move away from the dome in the opposite direction to the ridge.

[69] Comparison to the observed topography shows the following.

[70] 1. With $n = 2$, the amplitude of the variation in slope in the dome area is too small and the slope increases too much as we move away from the dome along the talweg.

[71] 2. With $n = 4$, it is the opposite; the amplitude of the variation in slope in the dome area is too high and the increase of the slope too low, especially for the weakest ridge.

[72] 3. With $n = 3$, both the amplitude of the variations in slope in the dome area and the variation of the slope on the left-hand side of the graph gives better results than with $n = 2$ and $n = 4$.

[73] We have shown in the previous experiments, that the slope pattern in the dome vicinity is only a function of Λ, and differs only a little as we move away from the dome, especially for the low values of ϵ. Consequently, by changing some of the parameters entering Λ (see equation (18)) for $n = 2$ or $n = 4$, we suppose it should be possible to obtain a

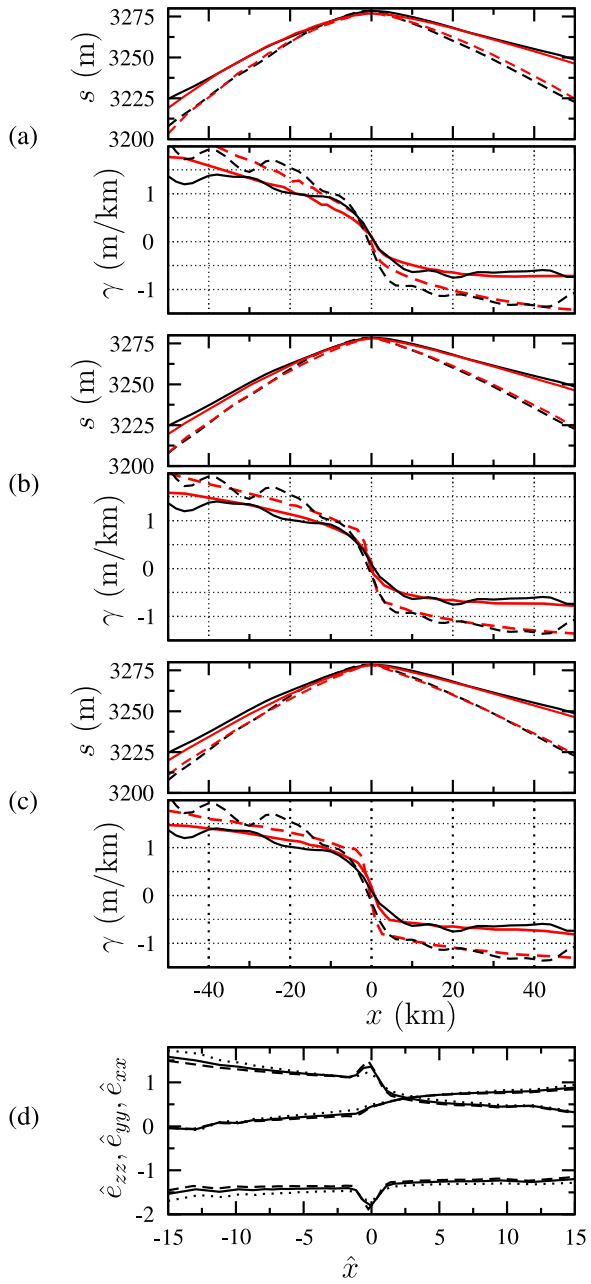

Figure 11. Experiment D2. Comparison of the surface elevation and slope obtained from a 5 km grid DEM of Greenland [*Bamber et al.*, 2001] (black lines) and from experiment D2 (red lines) at $\hat{t} = 0.017$ with (a) $n = 2$, (b) $n = 3$, and (c) $n = 4$. The modeled surfaces are shifted vertically by +280 m. (d) Comparison of the modeled surface longitudinal strain rates $\hat{e}_{xx}$, $\hat{e}_{yy}$, and $\hat{e}_{zz}$ along the ridge R2 obtained at $\hat{t} = 0.017$ with $n = 2$ (dotted lines), $n = 3$ (solid lines), and $n = 4$ (dashed lines). The results are given along the ridges R1 (solid lines) and R2 (diameter of the model) (dashed lines) (see Figure 10; x evolves according to the arrow and $x = 0$ is the junction of the two ridges).

better match of the model to the data either in the dome vicinity or away from the dome, but never everywhere.

[74] We remark that we compared the modeled results to the northern ridge because visually the matching of the surface contours plotted in Figure 10 is better. The southern ridge is a little bit sharper than the northern ridge but as we have seen with experiment B, the slope is more affected by n than by the other parameters. Comparison of the modeled surfaces with the southern ridge would lead to the same conclusions regarding the best choice of the Glen index to produce a match. For the same reason, we choose to compare the observed topography to our model results at time $\hat{t} = 0.017$ even if the steady state had not yet been reached, because our steady state ridges are more curved compared with the observed ridge. The differences in the topography pattern along the ridge R2 between $\hat{t} = 0.017$ and the steady state are very small, so that our conclusions remain valid and rheological information can still be inferred from the surface topography even when the dome is not in a steady state, at least if the changes in the boundary forcing are not too dramatic. This does not automatically implies that the surface of the Greenland Summit is not in a "near" steady state as different boundary forcings in our model would maybe lead to a less curved steady state ridge.

[75] The modeled surface longitudinal strain rates $\hat{e}_{xx}$, $\hat{e}_{yy}$ and $\hat{e}_{zz}$ along the ridge R2 obtained at $\hat{t} = 0.017$ with $n = 2$, $n = 3$ and $n = 4$ are shown in Figure 11d. As in the previous experiment, the strain rate state under the dome is not a uniaxial compression, and $\hat{e}_{xx} > \hat{e}_{yy}$. The higher vertical strain rate under the dome, which is due to the Raymond effect, is nearly all compensated for by a higher strain rate along the x direction $\hat{e}_{xx}$, while the effect on $\hat{e}_{yy}$ is very small. As already discussed, as n increases so does the horizontal variation of $\hat{e}_{zz}$ under the dome. During this period, the dome is still moving and the vertical strain rate is higher on the opposite side (left-hand side) of the weak ridge than under the weak ridge (right-hand side).

5. Conclusions

[76] The Raymond effect and especially the associated Raymond arches have previously been used to explore both the ice rheology and the formation/stability of ice ridges (see section 1 for references). Most of these applications are two-dimensional, which is suitable for modeling the flow of ice perpendicular to well-established ice ridges. However, for most ice domes, three-dimensional conditions prevail.

[77] We have used a three-dimensional finite element full-Stokes model to calculate the flow of ice under triple junctions. From a mathematical point of view, there is no evidence of spontaneous symmetry breaking at the flow center with the physical hypotheses we have adopted. Triple junctions are due to symmetry breaking in the far field. Thus, starting from an initially axisymmetric free surface, and applying a variable ice flux at the boundary, leads to the formation of a triple junction. In our experiments, it takes only few percent of the divide characteristic time for the triple junction to reach a stable topography.

[78] A 120° periodic forcing leads to the formation of a stable ideal triple junction at the origin where the dome is the meeting point of three identical ridges. The three ridges are straight and join the dome to the points at the boundary with the smallest ice flux. The Fletcher Promontory, presented in the companion paper, is close to that ideal.

[79] When we break the threefold symmetry, there is an initial time when ridges start to form from the points at the

boundary with the smallest ice flux. The initially axisymmetric dome, forms a triple junction first, then migrates to a stable position depending on the distribution of the ice fluxes at the boundary. The ridges can be curved, but, at the dome, the angle between the ridges is close to 120°.

[80] As expected, the smaller the along-ridge flux, the flatter the ridge in the along-flow direction and the sharper it is across the flow, with most of the deformation perpendicular to the ridge, with the situation approaching that of a plane-flow divide. By varying the magnitude of the ice fluxes at the boundary, we have modeled the case of a dome with two strong divides and one weak divide, and we have shown that it enters the family of the triple junctions, as it shares many similarities with the ideal triple junction regarding both the topography and the axial distribution of the Raymond effect. This seems to be the more general case for real ice sheets, as illustrated in this paper with the actual summit of Greenland, and in Part 2 with Thyssenhöhe, Berkner Island.

[81] The results presented here highlight this sharp decrease of the Raymond effect when we move away from the dome along a ridge. As previously shown by axisymmetric and 2.5-D models, the Raymond effect is at its maximum just under the dome and decreases quickly over a distance of less than one ice thickness. After this, the Raymond effect still operates under the ridges, but its magnitude depends on the along-ridge flow.

[82] This is associated with very high gradients in the slope and in the surface vertical strain rate, over one to two ice thicknesses in the dome area. Results obtained for divides where the dome is the highest point of a unique straight divide, not reproduced here, do not show these high gradients in the dome area when moving along the ridge. In this case, as expected, the Raymond effect decreases continuously beneath the divide as the along-ridge flow increases, but there is no clear distinction of the dome itself when looking at the slope and vertical strain rate patterns along the ridge. As a consequence, the general pattern for an isochronic surface under a triple junction is for a Raymond cupola to form under the summit, and for Raymond arch ridges to form under the arms. Real examples of such 3-D patterns are presented and discussed in the companion paper for Fletcher Promontory and Thyssenhöhe, Berkner Island.

[83] As a consequence of this change from near axisymmetry to strongly directional flow when a triple junction is present, the vertical surface strain rate varies strongly in the dome vicinity in every direction. The strain rate state varies also strongly in the dome vicinity from a uniaxial compression under the dome for a 120° symmetric triple junction to two-dimensional strain rate states, being longitudinal along the talweg and transverse under the ridges.

[84] We have shown that the slope gradient in the dome vicinity depends on the ice thickness, the accumulation, the ice fluidity and the Glen index. When scaled by Λ (equation (18)), which is a dimensionless parameter dependent on these quantities, the slope exhibits the same variations in the dome vicinity irrespective of the parameter choices. This pattern is the same for an isothermal ice sheet or for an ice sheet with a vertically stretched temperature profile. Consequently, knowing the ice thickness field and accumulation rate in principle allows us to determine the Glen index. The interest is that the surface reacts very quickly to new climatic conditions [*Hindmarsh*, 1996, 1997] and thus does not depend on the flow history as the Raymond arches do. Results of our model have been compared with the surface in the vicinity of the Greenland Ice Sheet summit, where Raymond arches are not observed, and a value of 3 for the Glen index gives a good match. This is the value used by large-scale SIA models that have been applied to the Greenland Ice Sheet [*Fabre et al.*, 1995; *Greve and Hutter*, 1995; *Huybrechts*, 1996].

[85] However, these applications raise several questions which need further exploration.

[86] 1. The shape, position and stability of the dome depend on large-scale effects; that is, in our model, on the ice fluxes far from the dome on the lateral boundary. Accurate modeling of the flow and evolution of the central parts of ice sheets then depends on accurate modeling of the margins of the ice sheets, and the ice fluxes at the boundary is the relevant information to pass from a large to a nested model. Up to now, the reciprocal effects of the small scale (dome position and shape) to the large scale have not been explored.

[87] 2. Local variations of the bedrock, sliding and accumulation are known to affect the flow of ice and the free surface and could affect our conclusions concerning the interpretation of the Glen index form the topography of triple junctions. Therefore, their effect on the slope in the dome vicinity has to be studied.

[88] 3. Studies have shown that anisotropy can affect the flow of ice and the Raymond effect [*Pettit et al.*, 2007; *Durand et al.*, 2007; *Gillet-Chaulet et al.*, 2006; *Martín et al.*, 2009a]. More efforts are needed in this direction to constrain the rheology of ice.

[89] 4. We have shown that modeling ice flow using isothermal and fixed temperature profiles can lead to the same surface but with very different vertical velocity profiles, so that a good matching of a modeled free surface with data does not necessarily imply a good matching of the vertical profiles. Consequently, data describing variation in the vertical direction, such as isochrones or strain rates are really needed to constrain models.

[90] **Acknowledgments.** Our thanks to Hugh Corr for advising us on the Greenland DEMs. This work was supported by NERC grant NE/F00446X/1, "Measuring and modeling the Raymond Effect for to infer low strain rate ice rheology." We thank Andy Aschwanden, Ed Waddington, and an anonymous reviewer for their detailed and thoughtful reviews.

References

Anandakrishnan, S., R. Alley, and E. Waddington (1994), Sensitivity of the ice-divide position in Greenland to climate change, *Geophys. Res. Lett.*, *21*(6), 441–444.

Bamber, J. L., R. L. Layberry, and S. P. Gogenini (2001), A new ice thickness and bed data set for the Greenland ice sheet: 1. Measurement, data reduction, and errors, *J. Geophys. Res.*, *106*, 33,773–33,780.

Clow, G. D., R. W. Saltus, and E. D. Waddington (1996), A new high-precision borehole-temperature logging system used at GISP2, Greenland, and Taylor Dome, Antarctica, *J. Glaciol.*, *42*, 576–584.

Dahl-Jensen, D., T. Thorsteinsson, R. Alley, and H. Shoji, (1997), Flow properties of the ice from the Greenland Ice Core Project ice core: The reason for folds?, *J. Geophys. Res.*, *102*, 26,831–26,840.

Dansgaard, W., et al. (1993), Evidence for general instability of past climate from a 250 kyr ice-core record, *Nature*, *364*, 218–220.

Doake, C. S. M., and E. W. Wolff (1985), Flow law in polar ice sheets, *Nature*, *314*, 255–257.

Dome-F Deep Coring Group (1998), Deep ice-core drilling at Dome Fuji and glaciological studies in east Dronning Maud Land, Antarctica, *Ann. Glaciol.*, *27*, 333–337.

Durand, G., F. Gillet-Chaulet, A. Svensson, O. Gagliardini, S. Kipfsthul, J. Meyssonnier, F. Parrenin, P. Duval, and D. Dahl-Jensen (2007), Change in ice rheology during climate variations—Implications for ice flow modelling and dating of the EPICA Dome C core, *Clim. Past*, *3*, 155–167.

EPICA Community Members (2004), Eight glacial cycles from an Antarctic ice core, *Nature*, *429*, 623–6284.

Fabre, A., A. Letréguilly, C. Ritz, and A. Mangeney (1995), Greenland under changing climates: Sensitivity experiments with a new three-dimensional ice sheet model, *Ann. Glaciol.*, *21*, 1–7.

Fowler, A. C. (1992), Modelling ice sheet dynamics, *Geophys. Astrophys. Fluid Dyn.*, *63*, 29–65.

Gagliardini, O., and J. Meyssonnier (2000), Simulation of anisotropic ice flow and fabric evolution along the GRIP-GISP2 flow line (Central Greenland), *Ann. Glaciol.*, *30*, 217–223.

Gagliardini, O., and T. Zwinger (2008), The ISMIP-HOM benchmark experiments performed using the finite-element code Elmer, *Cryosphere*, *2*, 67–76.

Gillet-Chaulet, F., O. Gagliardini, J. Meyssonnier, T. Zwinger, and J. Ruokolainen (2006), Flow-induced anisotropy in polar ice and related ice-sheet flow modelling, *J. Non-Newt. Fluid Mech.*, *134*, 33–43.

Glen, J. W. (1955), The creep of polycrystalline ice, *Proc. R. Soc. London, Ser. A*, *228*, 519–538.

Greve, R., and K. Hutter (1995), Polythermal three-dimensional modelling of the Greenland ice sheet with varied geothermal heat flux, *Ann. Glaciol.*, *21*, 8–12.

Gundestrup, N. S., D. Dahl-Jensen, S. J. Johnsen, and A. Rossi (1993), Bore-hole survey at dome GRIP 1991, *Cold Reg. Sci. Technol.*, *21*, 399–402.

Hindmarsh, R. C. A. (1996), Stochastic perturbation of divide position, *Ann. Glaciol.*, *23*, 93–104.

Hindmarsh, R. C. A. (1997), Normal modes of an ice sheet, *J. Fluid. Mech.*, *335*, 393–413.

Hindmarsh, R. C. A., E. C. King, R. Mulvaney, H. F. J. Corr, and F. Gillet-Chaulet (2011), Flow at ice-divide triple junctions: 2. Three-dimensional views of isochrone architecture from ice-penetrating radar surveys, *J. Geophys. Res.*, doi:10.1029/2009JF001622, in press.

Hutter, K. (1983), *Theoretical Glaciology: Material Science of Ice and the Mechanics of Glaciers and Ice Sheets*, D. Reidel, Dordrecht, Netherlands.

Huybrechts, P. (1996), Basal temperature conditions of the Greenland ice sheet during the glacial cycles, *Ann. Glaciol.*, *23*, 226–236.

Hvidberg, C. S. (1996), Steady-state thermomechanical modelling of ice flow near the centre of large ice sheets with the finite-element technique, *Ann. Glaciol.*, *23*, 116–123.

Hvidberg, C. S., D. Dahl-Jensen, and E. D. Waddington (1997), Ice flow between the GRIP and GISP2 boreholes in Central Greenland, *J. Geophys. Res.*, *102*, 26,851–26,859.

Jacobel, R. W., and S. J. Hodge (1995), Radar internal layers from the Greenland Summit, *Geophys. Res. Lett.*, *22*, 587–590.

Le Meur, E., O. Gagliardini, T. Zwinger and J. Ruokolainen (2004), Glacier flow modelling: A comparison of the Shallow Ice Approximation and the full Stokes Solution, *C. R. Phys.*, *5*, 709–722.

Lipenkov, V. Y., A. N. Salamatin, and P. Duval (1997), Bubbly-ice densification in ice sheets: II. Applications, *J. Glaciol.*, *43*, 397–407.

Lliboutry, L., and P. Duval (1985), Various isotropic and anisotropic ices found in glacier and polar ice caps and their corresponding rheologies, *Ann. Geophys.*, *3*, 207–224.

Mangeney, A., F. Califano, and O. Castelnau (1996), Isothermal flow of an anisotropic ice sheet in the vicinity of an ice divide, *J. Geophys. Res.*, *101*, 28,189–28,204.

Marshall, S. J., and K. M. Cuffey (2000), Peregrinations of the Greenland Ice Sheet divide in the last glacial cycle: Implications for central Greenland ice core, *Earth Planet. Sci. Lett.*, *179*, 73–90.

Martín, C., R. C. A. Hindmarsh, and F. J. Navarro (2006), Dating ice flow change near the flow divide at Roosevelt Island, Antarctica, by using a thermomechanical model to predict radar statigraphy, *J. Geophys. Res.*, *111*, F01011, doi:10.1029/2005JF000326.

Martín, C., G. H. Gudmundsson, H. D. Pritchard, and O. Gagliardini (2009a), On the effects of anisotropic rheology on ice flow, internal structure, and the age-depth relationship at ice divides, *J. Geophys. Res.*, *114*, F04001, doi:10.1029/2008JF001204

Martín, C., R. C. A. Hindmarsh, and F. J. Navarro (2009b), On the effects of divide migration, along-ridge flow, and basal sliding on isochrones near an ice divide, *J. Geophys. Res.*, *114*, F02006, doi:10.1029/2008JF001025.

Mulvaney, R., O. Alemany, and P. Possenti (2007), The Berkner Island (Antarctica) ice-core drilling project, *Ann. Glaciol.*, *47*, 115–124.

Nereson, N. A., and C. F. Raymond (2001), The elevation history of ice streams and the spatial accumulation pattern along the Siple Coast of West Antarctica inferred from ground-based radar data from three inter-ice-stream ridges, *J. Glaciol.*, *47*, 303–313.

Nereson, N. A., and E. D. Waddington (2002), Isochrones and isotherms beneath migrating ice divides, *J. Glaciol*, *48*(160), 95–108.

Nereson, N. A., R. C. A. Hindmarsh, and C. F. Raymond, (1998a), Sensitivity of the divide position at Siple Dome, West Antarctica to boundary forcing, *Ann. Glaciol.*, *27*, 207–214.

Nereson, N. A., C. F. Raymond, E. D. Waddington, and R. W. Jacobel (1998b), Migration of the Siple Dome ice divide, West Antarctica, *J. Glaciol.*, *44*, 643–652.

Nereson, N. A., C. F. Raymond, R. W. Jacobel, and E. D. Waddington (2000), The accumulation pattern across Siple Dome, West Antarctica, inferred from radar-detected internal layers, *J. Glaciol.*, *46*, 75–87.

Nye, J. F. (1991), The topology of ice-sheet centers, *J. Glaciol.*, *37*, 220–227.

Parrenin, F., and R. C. A. Hindmarsh (2007), Influence of a non-uniform velocity field on isochrone geometry along a steady flowline of an ice sheet, *J. Glaciol.*, *53*, 612–622.

Parrenin, F., et al. (2007), 1-D-ice flow modelling at EPICA Dome C and Dome Fuji, East Antarctica, *Clim. Past*, *3*, 243–259.

Pattyn, F. (2008), Investigating the stability of subglacial lakes with a full Stokes model. *J. Glaciol.*, *54*, 353–361, doi:10.3189/002214308784886171.

Pettit, E. C., and E. D. Waddington (2003), Ice flow at low deviatoric stress, *J. Glaciol.*, *49*, 359–369.

Pettit, E. C., T. Thorsteinsson, H. P. Jacobson, and E. D. Waddington (2007), The role of crystal fabric in flow near an ice divide, *J. Glaciol.*, *53*, 277–288.

Price, S. F., H. Conway, and E. D. Waddington (2007), Evidence of late Pleistocene thinning of Siple Dome, West Antarctica, *J. Geophys. Res.*, *112*, F03021, doi:10.1029/2006JF000725.

Raymond, C. F. (1983), Deformation in the vicinity of ice divides, *J. Glaciol.*, *29*, 357–373.

Ritz, C., V. Rommelaere, and C. Dumas (2001), Modeling the evolution of Antarctic ice sheet over the last 420,000 years: Implications for altitude changes in the Vostok region, *J. Geophys. Res.*, *106*, 31,943–31,964.

Thorsteinsson, T., and E. D. Waddington (2002), Folding in strongly anisotropic layers near ice-sheet centers, *Ann. Glaciol.*, *35*, 480–486.

Vaughan, D. G., H. F. J. Corr, C. S. M. Doake, and E. D. Waddington (1999), Distortion of isochronous layers in ice revealed by ground-penetrating radar, *Nature*, *398*, 323–326.

Vialov, S. S. (1958), Regularities of glacial shields movement and the theory of plastic viscous flow, in *Physics of the Motion of the Ice*, *IASH Publ.*, vol. 47, pp. 266–275, IAHS Press, Wallingford, U. K.

Wilchinsky, A. V., and V. A. Chugunov (1997), Modelling ice-divide dynamics by perturbation methods, *J. Glaciol.*, *43*, 352–358.

Zwinger, T., R. Greve, O. Gagliardini, T. Shiraiwa, and M. Lyly (2007), A full Stokes-flow thermo-mechanical model for firn and ice applied to the Gorshkov crater glacier, Kamchatka, *Ann. Glaciol*. *45*, 29–37.

F. Gillet-Chaulet and R. C. A. Hindmarsh, Physical Sciences Division, British Antarctic Survey, Natural Environment Research Council, High Cross, Madingley Road, Cambridge CB3 0ET, UK. (fall@bas.ac.uk; rcah@bas.ac.uk)